Automation in Construction 145 (2023) 104626

Contents lists available at ScienceDirect

Automation in Construction

journal homepage: www.elsevier.com/locate/autcon

Modelling the influence of material and process parameters on Shotcrete 3D Printed strands - cross-section adjustment for automatic robotic manufacturing

Lukas Lachmayer [a,*], David Böhler [b], Niklas Freund [b], Inka Mai [b], Dirk Lowke [b], Annika Raatz [a]

[a] match, Leibniz Universität Hannover, An der Universität 2, Garbsen 30823, Niedersachsen, Germany
[b] Institute of Building Materials, Concrete Construction and Fire Safety, TU Braunschweig, Beethovenstr. 52, Braunschweig 38106, Niedersachsen, Germany

ARTICLE INFO

Keywords:
3D concrete printing
Process control
Additive manufacturing in construction
Shotcrete 3D printing
Flexural strength
Geometry
Material and process parameters
Robot based manufacturing

ABSTRACT

Due to its high interlayer strength and application flexibility, Shotcrete 3D Printing (SC3DP) is a promising method for the additive manufacturing of structural concrete components. The printing process is based on a layer-wise material application, conducted along a pre-designed printing path. However, material batch inhomogeneities and environmental alteration lead to varying concrete properties over the production processes. These material irregularities stochastically affect the layer geometry and thus limit the achievable reproducibility and accuracy. To enhance the process stability and improve the dimensional component quality in case of environmental changes, a reliable mapping between the strand geometry and the process and material parameters is fundamental for systematic cross-section adjustment.

In this paper, we present an experimental-based approach for attaining a flexible regression model of the cross-section of Shotcrete 3D Printed concrete strands. The width and height of the layer are chosen for the strand representation, which we considered as the main factors for the printing-path planning. Regarding the modelling parameters, we focus on the volume flow parameters of concrete and air, and on the accelerator dosage. These inertia afflicted parameters can provide a consistent strand geometry, while factors of lower latency such as printing speed or spray distance are conserved for online adaptation. Based on the presented proceeding, an adjustable layer height and width model has been successfully used to predict the strand properties. The production of a medium sized sample wall further proves the applicability to the production process. In addition, we demonstrated that the chosen parameters not only affect the geometry but also the mechanical performance of SC3DP-specimens. This is evaluated based on flexural strength measurements. Given the geometrical and mechanical properties, the study defines applicable limits for the investigated parameters.

1. Introduction

Skilled labour shortages [1], resource wastage due to inefficient use of materials, and environmental pollution due to high waste rates and energy consumption are currently among the biggest challenges of the construction industry [2,3]. These are increasingly countered by the development of highly automated production processes. The main scope is to reduce the number of skilled manual activities, achieve greater efficiency through the optimized use of cost-intensive materials, and reduce wastage [4,5]. However, only hesitant adaptation or replacement of proven manufacturing processes can be observed within the industrial application. Main reasons for the slow pace of change are the low lot sizes due to customization and the large number of co-entrepreneurs in construction projects, leaving only small margins for investigating unapproved changes [6,7].

Taking into account the industrial concerns and the overall challenges, the development of robust, fully automated production process seems necessary. In this regard, the degree of automation, the ability of mass customization, and the capability of prefabrication of additive manufacturing (AM) processes show great potential to overcome the current weaknesses of the construction industry [8,9]. Investigating existing techniques reveals that most of the benefits of additive manufacturing processes are correlated to high resolution printing and fast material setting times. While the former enables production of

* Corresponding author.
E-mail address: lachmayer@match.uni-hannover.de (L. Lachmayer).

https://doi.org/10.1016/j.autcon.2022.104626
Received 19 July 2022; Received in revised form 31 August 2022; Accepted 12 October 2022
Available online 1 November 2022

complex shapes, topology optimized components, and overhangs, the latter ensures component stability throughout the printing process.

Due to the slowly evolving yield stress of fresh concrete, common concrete mixtures do not fulfill the prerequisite of fast material setting times. Therefore, a one-to-one use of existing 3D printing processes limits either the build volume, when utilizing self-supporting powder bed approaches, or the producible component complexity when using free-form extrusion or jetting methods. In this regard, sample studies have shown that the inclination for concrete extrusion is limited to 25 % of the values, achievable with polymers [10,11]. In addition, the bond strength between the extruded layers can significantly limiting the final load bearing capacity of 3D printed parts [12–15].

Shotcrete 3D Printing (SC3DP) is characterized by high build up rates, improved layer interlocking, and, due to the material jetting, offers a high geometrical freedom in terms of producible overhangs, or even overhead operation [16,17]. Although SC3DP potentially enables AM in construction, it offers new challenges compared to traditional concrete casting. Especially, since the resulting hardened state properties such as strand geometry or mechanical performance do not necessarily meet the targeted values due to noise in process parameters, variation in mixture composition, and changing environmental conditions [18,19]. However, for the printing path planning, such inconsistencies cannot be respected leading to deviations between as-planned and as-printed geometries. Consequently, realising the envisaged strand properties from the planning process, in particular the height h_L and the width w_L of the layer, is of utmost interest to ensure the intended material application, and thus to guarantee high dimensional product quality and printing as planned.

Therefore, a profound understanding of material-process-interactions is required. As a first step, this understanding enables to adapt material and process to specific requirements and facilitates off-line path planning. In a second step, process parallel acquired sensor data can serve as a basis for an automated control for the entire system in the future. For the first step, it is of high importance to gain an understanding of how to modify process parameters in order to change the geometry considering the effect this has on the hardened properties, i.e. mechanical strength, of the produced concrete components. Only when considering material and process-related aspects, an automation of the process is feasible for future applications.

In this paper, we investigate the adjustability of the shotcrete strand to achieve a model based strand cross-section prediction based on empirical process investigations. Therefore, we first aim to determine the influences of flow rates and material parameters towards the layer geometry. We use a three level face centred design of experiments (DoE) to identify potential effects of the parameters on the strand's geometry. Based on the DoE we build and reduce a multi-linear regression model to predict the strand properties for the production processes. To compensate day-to-day production inconsistencies, we samplewise update the model for a second production run. The resulting model is tested by manufacturing a sample component. Furthermore, the effect of process and material parameters on interlayer strength is shown via flexural strength investigations.

2. Materials and methods

Within the following subsections we provide fundamentals about our manufacturing process, the utilized modelling approach, as well as the experimental setup and data acquisition.

2.1. Shotcrete 3D Printing SC3DP and its adjustable parameters

Prior to modelling the influences of the process and material parameters on the strand geometry, a detailed investigation of the manufacturing process and possible influencing variables is required.

2.1.1. Shotcrete 3D Printing

SC3DP is a novel AM technology developed at TU Braunschweig [21]. It is based on an automated wet-mix shotcrete process [22]. A detailed description of our setup is given in section 2.3.2. According to the RILEM process classification framework for digital fabrication with concrete, SC3DP can be classified to the process sub-class 'material jetting' [23]. In contrast to the widely established material extrusion techniques, SC3DP uses pressurized air to apply the material with a defined distance between nozzle and strand. Due to the application with high kinetic energy, the applied material is highly compacted which results in a good interlocking between the printed layers. Thus, the risk of cold joints between the layers is significantly minimized [16,24]. Due to its spray application, a high degree of freedom regarding the nozzle orientation is possible. Therefore, robotic guided SC3DP allows real three-dimensional processing. Fig. 1a) shows the robot based SC3DP according to [20].

2.1.2. Parameters to adjust the SC3DP result

In contempt of the material properties and environmental influences there are at least nine tunable parameters which affect the process result of SC3DP [25], see Fig. 1b). As presented in Fig. 1c) those include the volume flow rates for air $\dot{v}_{air}$, for concrete $\dot{v}_{con}$ and the accelerator dosage Dos_{acc}. Furthermore the nozzle velocity v_N, the nozzle distance d_N and the application angle α_N, and in addition the nozzle bore diameter b_N, and the layer number n_L and layer angle β_L will also change the cross-section of the applied strand.

According to Fig. 1c), we initially classify the process parameters based on controllability. The first level consists of the, by-now, non-online-controllable factors such as the layer number and the layer inclination angle. Both are determined by the printing object and the process related print path planning [27]. This category also includes the nozzle bore diameter [16]. The second level of parameters is characterized by a dead-time behaviour and the influence of the parameters on the resulting mechanical properties of the component. This includes all volume flow and dosage parameters; hence the conveyance through pipes and hoses, as well as valve actuation, requires a considerable amount of time in terms of control. The third level includes online controllable process parameters as nozzle feed rate, nozzle distance, and application angle, which can be adjusted during the process by overwriting the printing path settings. Table 1 provides a summarising list of parameters affecting the SC3DP result.

Recent studies have shown that these parameters not only affect the strand geometry but can have a significant effect on the structural build-up, and thus on the buildability [16,26]. Therefore, they are principally suitable as adjustment option for the SC3DP process. However, it must also be taken into account that these parameters affect the hardened concrete properties, such as the interlocking between the layers [16]. Thus, we include material-based quality investigations in the development of the model in order to define sensible variation limits.

2.1.3. State of the art - process parameter investigations and modelling

Modelling the influences of printing and material parameters of the shotcrete process is not solely of interest for SC3DP. First research experiments on shotcreting are given by the field of tunnel construction which initially used the process for reinforcement. Early experiments focused on the impact of d_N, v_N and an additional rotational nozzle oscillation while spraying concrete. In order to achieve a homogeneous strand, d_N was recommended to be above 1 *m* and v_N should not raise above 9.000 *mm/min* [28]. Additional multilayer experiments were carried out to further predict the evenness when applying several layers. A reduced layer height shows an improved final surface [29]. While these attempts proved the adjustability of the strand geometry by parameter variation, the resulting layer width of 750 *mm* is significantly above the width values required for 3D printing of structural components.

Ginouse et al. [30] deliver fundamentals to strand geometry

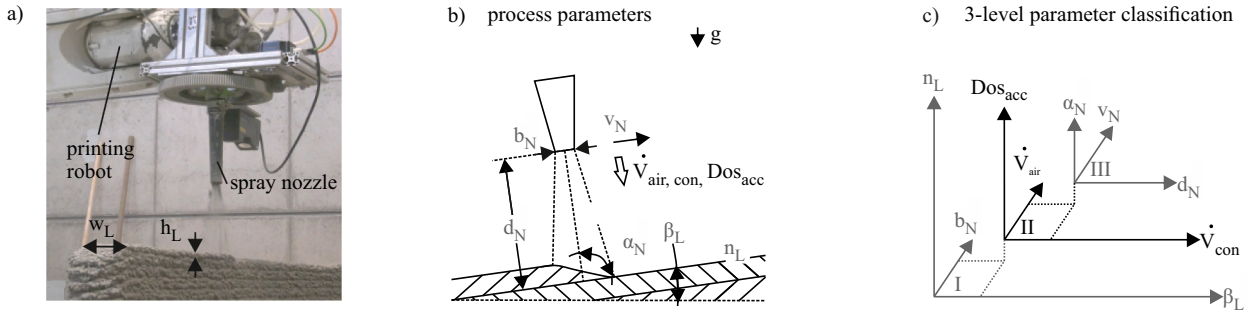

Fig. 1. a) Robotic Shotcrete 3D Printing process [20] b) Main parameters which are influencing the strand geometries: nozzle distance d_N, nozzle bore diameter b_N, nozzle feed rate v_N during printing, volume flow rate air $\dot{v}_{air}$, volume flow rate concrete $\dot{v}_{con}$, accelerator dosage Dos_{acc}, nozzle angle α_N to previous layer, layer angle β_L, and layer number n_L c) Parameter classification according controllability and dead-time behaviours.

Table 1
Summary of shotcrete process parameters [25,26].

	Parameter	Unit	Level
n_L	layer number		I
β_L	layer angle	°	I
b_N	bore diameter	mm	I
$\dot{v}_{air}$	air volume flow	m^3/h	II
$\dot{v}_{con}$	concrete volume flow	m^3/h	II
Dos_{acc}	accelerator dosage	% of binder	II
α_N	application angle	°	III
v_N	nozzle feed rate	mm/min	III
d_N	nozzle distance	mm	III

prediction by examining the influences of the process parameters to the material distribution. A 2^{nd} order gaussian distribution is proposed as a material application model. To validate the model, multiple spraying tests were carried out during tunnel construction without nozzle movement. The sprayed material was collected enabling inspection of the allocation. The resulting model predicts h_L for a single layer with an error of 15 %. By applying the model to a shotcrete process with surrounding formwork, prediction of the layer height up to four layers was validated [31]. However, regarding up-scaled printing processes without formwork, 15 % error per layer would result in severe deviations.

Further modelling approaches focused on the dependencies between h_L and w_L as well as the printing and material parameters [26]. During these investigations d_N was raised from 150 *mm* to 300 *mm*, and showed a linear width increase as well as a linear height decrease. Similar linear relations were examined when varying $\dot{v}_{air}$, which lead to a width increase when higher air flows are used. Additionally, the strand geometry can be changed through the accelerator dosage Dos_{acc}. For a range from 0 to 6 Dos_{acc} [%] accelerator, a linear increase of the layer height was measured [25,26]. Given these results we state that, first h_L and w_L are identified as the most significant parameters to classify the shotcrete strand and, ultimately, linear correlations between the adjustable parameters and the process results must be considered. However, no repetition experiments were investigated and the applicability of the dependencies towards modelling of the correlations is not validated.

Recent investigations used vertical surfaces to further study the correlations [32]. The height h_L will be reduced when either the printing speed v_N or the spray distance d_N is increased. On the opposite, the layer width w_L raises. A trapezoidal model was build, assuming an additional combined influence of $\dot{v}_{con}$ and v_N for the locally deposited material, as well as linear influences of d_N and $\dot{v}_{con}$ to the strand cross-section. Although the model can represent a single layer geometry on vertical surfaces, the deviations between the measured data and the model prediction are up to 20 %. Despite the inaccuracy, this study indicates that for further modelling approaches to predict the layer height and width, besides linear influences, the interactions between the process parameters must be considered.

2.2. Geometrical modelling approach

Taking into account the prediction accuracy of previous studies, 3D printing with such values will result in severe height deviations. While our modelling approach also focuses on layer height h_L and layer width w_L, we aim for a straightforward model, to enable considering varying environmental variations by fast recalibration. For model building itself we use linear relationships, as well as the influences of the interactions between the process parameters. Moreover, the mechanical properties, which will also be influenced by the variation of the process parameters and affect the buildability, are considered when defining process boundaries.

2.2.1. Derivation of the SC3DP process parameters for the experiments

To achieve adaptability and recalibration we need to limit the required experiments by select sensible process parameters. Regarding the parameters in Fig. 1c), we focus on the level II volume flow rates $\dot{v}_{air}$ $[m^3/h]$, $\dot{v}_{con}$ $[m^3/h]$ and dosage Dos_{acc} [%]. On the one hand, this is due to the fact that the first level of parameters is defined during the print path planning and uncontrollable within our system; and on the other, the geometry effects of third level parameters will depend on the chosen flow rates and dosages, and they are useful for online control in the future.

As guideline for the parameter settings, the parameter ranges were selected along previous investigations [26] and set according to the values given in Table 2. All other non-investigated parameters were kept constant according to the values given in Table 3. Based on [25,26], these values are suitable for SC3DP.

2.2.2. Mathematical model description

Modelling the relationships between the chosen process parameters and the strand geometries, at first requires a quantitative description of the result. Since the focus is placed on the layer height h_L and the layer width w_L, we state the following assumptions, based on section 2.1.3.

$$w_L = f\left(\dot{v}_{air}, \dot{v}_{con}, Dos_{acc}\right) \tag{1}$$

$$h_L = f\left(\dot{v}_{air}, \dot{v}_{con}, Dos_{acc}\right) \tag{2}$$

Table 2
Range of investigated volume flow and dosage parameters.

Parameter	Minimum	Maximum
$\dot{v}_{air}$ [m^3/h]	30	50
$\dot{v}_{con}$ [m^3/h]	0.4	0.8
Dos_{acc} [%]	0	6

Table 3
Constant process parameters and settings during the experiments.

Parameter	Setting
n_L []	1–5
b_N [mm]	15
β [°]	0
α [°]	90
v_N [mm/min]	4500
d_N [mm]	200

With regard to the depicted linear and combined influences of the parameters, as well as our goal for an adaptable model, a multi-linear regression seems suitable. Such an approach provides flexible correlations between the process parameters and ensures a limited number of model parameters, which consequently limits the amount of required calibration experiments. Thus, we utilize the quadratic model from [33], and added our parameters so the equation results in (3) and (4), in order to describe the layer width and height.

$$\begin{aligned} w_L &= k_{w0} \\ &+k_{w1}\dot{v}_{air} + k_{w2}\dot{v}_{con} + k_{w3}Dos_{acc} \\ &+k_{w4}\dot{v}_{air}\dot{v}_{con} + k_{w5}\dot{v}_{air}Dos_{acc} + k_{w6}\dot{v}_{con}Dos_{acc} \\ &+k_{w7}\dot{v}_{air}^2 + k_{w8}\dot{v}_{con}^2 + k_{w9}Dos_{acc}^2 \end{aligned} \tag{3}$$

$$\begin{aligned} h_L &= k_{h0} \\ &+k_{h1}\dot{v}_{air} + k_{h2}\dot{v}_{con} + k_{h3}Dos_{acc} \\ &+k_{h4}\dot{v}_{air}\dot{v}_{con} + k_{h5}\dot{v}_{air}Dos_{acc} + k_{h6}\dot{v}_{con}Dos_{acc} \\ &+k_{h7}\dot{v}_{air}^2 + k_{h8}\dot{v}_{con}^2 + k_{h9}Dos_{acc}^2 \end{aligned} \tag{4}$$

Within this equations, $k_{w,\,h1\ldots9}$ describe constant values which either have to be calculated with respect to width for $k_{w1\ldots9}$, or height for $k_{h1\ldots9}$. According to multi-linear regression, these factors will be dimensionless and the model input volume flows and dosage must be scaled to a range from −1 to 1. Reducing the real volume flow rates to zero, the correlated model values drop to −1 and compensate for the constant layer property offsets $k_{w,\,h0}$, which otherwise would indicate a dimension without a volume flow.

2.3. Experimental setup and data acquisition

When converting the modelling approach into a solvable equation system, at least ten tests must be performed to calculate the parameters $k_{w,\,h,\,0\ldots9}$. To determine the individual test settings for each experiment, we referred to a face-centred design of experiments. This is for example shown in Fig. 2 for the chosen process parameters.

The design of experiments ensures a statistically independent identification of the proposed model parameters. However, according to the DoE rules, we have to generate a series of 15 experiments. Taking into account the predefined parameter limits from Table 2, we chose the settings for our experiments according to the numbers given in Table 4.

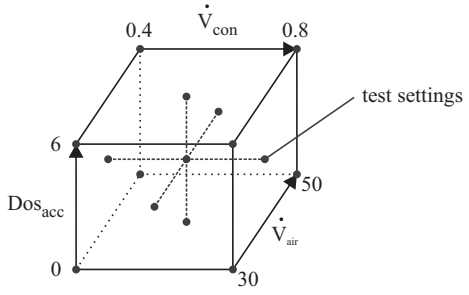

Fig. 2. Face-centred DoE-plan according to the chosen parameter settings given in Table 4.

Table 4
Investigated parameter settings for the face centred design of experiments.

No.	$\dot{v}_{con}$ [m^3/h]	Dos_{acc} [%] / [l/h]	$\dot{v}_{air}$ [m^3/h]
$08_{con}6_{acc}50_{air}$	0.8	6 / 17.52	50
$08_{con}6_{acc}30_{air}$	0.8	6 / 17.52	30
$08_{con}3_{acc}40_{air}$	0.8	3 / 8.76	40
$08_{con}0_{acc}50_{air}$	0.8	0 / 0.00	50
$08_{con}0_{acc}30_{air}$	0.8	0 / 0.00	30
$06_{con}6_{acc}40_{air}$	0.6	6 / 13.14	40
$06_{con}3_{acc}50_{air}$	0.6	3 / 6.57	50
$06_{con}3_{acc}40_{air}$	0.6	3 / 6.57	40
$06_{con}3_{acc}30_{air}$	0.6	3 / 6.57	30
$06_{con}0_{acc}40_{air}$	0.6	0 / 0.00	40
$04_{con}6_{acc}50_{air}$	0.4	6 / 8.76	50
$04_{con}6_{acc}30_{air}$	0.4	6 / 8.76	30
$04_{con}3_{acc}40_{air}$	0.4	3 / 4.38	40
$04_{con}0_{acc}50_{air}$	0.4	0 / 0.00	50
$04_{con}0_{acc}30_{air}$	0.4	0 / 0.00	30

The numbering *no.* was performed by combining the values for $\dot{v}_{con}$, Dos_{acc} and $\dot{v}_{air}$. This enumeration is kept for further descriptions. While the first layer is printed on a hard surface, the following layers are sprayed on fresh concrete. We assume this will reduce the spreading of the material because the hardness of the substrate decreases with an increasing number of layers. We therefore decided to also take into account the layer number and evaluate the material behaviour up to five layers.

2.3.1. Mixture composition and preparation

For the study, a polymer modified mortar provided by MC-Bauchemie Müller GmbH & Co. KG, Bottrop, Germany developed for spraying applications was used. The mixture composition is given in Table 5. The binder phase consists of an Ordinary Portland Cement (OPC, CEM I 52.5 R according to EN 197–1) and two different pozzolans. Quartz sand with a maximum grain size of 2 *mm* was used as aggregate. In addition, the mixture contains pulverized chemical admixtures.

For the experiment, batches with 100 *kg* of dry powder and the corresponding amount of 14 *l* of water are prepared in two compulsory mixers (Mader WM Jetmix 125/180, Erbach, Germany). For that, water and the dry components were added into the container while the mixing tool was rotating. In total, the mixing took 4 min per batch. Both mixers were time shifted by 2 min in order to provide a continuous material flow for the SC3DP-process. For quality control, a flow table test (according to to DIN EN 12350–5) is taken on a regular basis as a quality control measure. The flow table test resulted in f = 40 *cm* ± 5.9 *cm*.

2.3.2. Material processing in the digital building fabrication laboratory (DBFL)

The experiments presented within this study were carried out at the Digital Building Fabrication Laboratory (DBFL). The DBFL is one of the facilities available at TU Braunschweig to manufacture with SC3DP. It is based on a gantry system equipped with two 3-axis portals extended by a 6-axis Stäubli TX200 industrial robot, which is used to guide the Shotcrete 3D Printing nozzle. A 5-axis CNC gantry can be used for cooperative tasks such as the integration of reinforcement elements [24].

The system provides a total workspace of 10.50 · 5.25 · 2.50 m^3 and is controlled via a Sinumerik 840D. For motion planning, the printing path

Table 5
Mix proportions of the concrete used for 3D printing; all numbers have the unit kg/m^3.

OPC	500
Pozzolan	160
Silica Fume	25
Sand	1180
Water	266
pulverized admixtures, fibers	33

is designed within Rhinoceros3d using Grasshopper, and simulated with a virtual model of the production system. In combination with the "Robots" plugin, additional informations, such as concrete pump activation commands for the material production line, are added at dedicated path points. Afterwards, the automatically generated G-Code files are transferred to the Sinumerik control and executed to run the system. The material production line itself is controlled by an additional industrial PC from Beckhoff Automation. This unit receives the mixing and conveying commands from the Sinumerik and manages a WM-variojet FU concrete pump (Werner Mader GmbH) as well as multiple valves for volume flow and dosage control. The material mixing is performed according to section 2.3.1. To transfer the material from the pump to the printing nozzle, 25 *m* of hoses with a diameter of 35 *mm* are installed. For all experiments we used a printing nozzle with a diameter of 15 *mm*.

2.3.3. Specimen design for geometric investigations

Conduction of all experiments within one run is necessary to guarantee steady external conditions. To overcome the limited machine working space, a specific specimen design was developed. As can be seen in Fig. 3, we utilized a pyramidal layout which enables individual investigation each of the five layers. This beneficially allows to take into account the layer number during data evaluation. However, the nozzle feed rate is not constant during the transition between the layers, so these segments must not be used for the evaluation process. The length of these transition areas is assumed to be approximately 200 *mm* including a security margin of 25 *mm* to both sides. The total length of the specimens is 2200 *mm*. Thus, deducting the transition areas, the remaining length for each evaluation area is 200 *mm*. Fig. 3 also shows the hardened pyramidal specimens within the workspace. The material agglomerations at the end of each layer step show the effect of the inconsistent feed rate in the transition areas.

2.3.4. Interlayer bond strength

The qualitative investigation of the interlayer bond strength was carried out by testing the flexural strength of prisms. For this purpose, specimens with 4 layers were printed according to Fig. 4 (left). Approximately 2 weeks after production, prisms perpendicular to the layer direction are cut. The impact of cutting was minimized by using a fine saw blade. Since a length of 160 *mm* could not be realized for every sample, a few samples are elongated by adding concrete in a subsequent process (Fig. 4 - right). The prisms $160 \cdot 40 \cdot 40\ mm^3$ are tested after 28 days with a loading parallel to the layer direction in a 3-point bending test. The interface layers were positioned in the middle so that the highest bending moment was applied in between two layers, Fig. 4. Specimen, which failed at another location than in the middle third (e.g. failure at the adhesive joint between the specimen and the subsequently added concrete) were considered invalid and were not evaluated.

2.4. Geometrical data acquisition and processing

The specimen surfaces exhibit slight variations due to the distribution of the aggregate size. Thus, human based sample wise data acquisition would allow only a partial representation of the specimen. To realize a statistically valid evaluation of the produced specimens, we aimed for a high resolution fully-automatic digitalization of the strands, to enable a comprehensive investigation of the geometric strand properties.

2.4.1. Scanner unit

Core element of our data acquisition is a 2D-Laser-Scanner attached to the production robot and moved along the pre-produced specimens. To keep the laser line perpendicular to the printing direction of the specimens, a 360° endless rotational unit was constructed. As can be seen in Fig. 5, the unit consists of a slewing ring, a slip ring and a stepper motor, where the ring diameter allows central positioning of the printing nozzle. The utilized Keyence LJ-X 8400 laser sensor head offers a measurement range of 315 *mm* in the vertical axis and a maximum range of 320 *mm* along the horizontal direction. The repeatability in height is about 5 μm and the resolution along the width of the specimens is 10 μm. To obtain a sufficient resolution, we performed a scan every 4 *mm* along the 2.200 *mm* specimens, two days after production.

2.4.2. Error correction and levelling

The presented data in Fig. 6a) belongs to specimen no. $08_{con}6_{acc}50_{air}$. It shows, that the raw scanner data contains the unintended transition areas between the layers as well as measurement errors, caused by reflections. Since those are not representative for the strand properties they must be excluded from the data sets. While the reflections can be identified via the specific error values, we implemented an additional algorithm for the systematic extraction of the transition areas. The algorithm is based on the derivation of the maximum height values. Within this derivation, the transition areas are highlighted as two minima and three maxima of gradient, depicted as green crosses in Fig. 6b). To eliminate the transition areas, 25 of the recorded profiles in the direction of the specimen center are deleted, starting from the minima and the maxima of the gradient. Additionally, the algorithm corrects the inclination of the printing surface. This is done by fitting a plane through outmost points of each of the recorded data sets. We then calculate the plane value at each length-width-coordinate of the measurement points. Afterwards, the measured height-values are reduced by the distance between the correlated plane value and the smallest value of the measured data set. Fig. 6c) shows the adjusted data set for the sample specimen from Fig. 6a). For the further evaluation of the layer height and width within each of the the prepared data sets, we describe an additional algorithm within the next section.

2.4.3. Height and width evaluation algorithm

To identify the width of the specimens within the scanner data, we calculate the derivation of the recorded cross-sections. As can be seen in Fig. 7a) the maxima and minima of the derivation clearly mark the left and right border of the material strand. To define the strand height we compute the mean average in between the left and the right boundary. However, depending on the scanner data, the flanks of the material strand are randomly included in the height evaluation. E.g. for Fig. 7a)

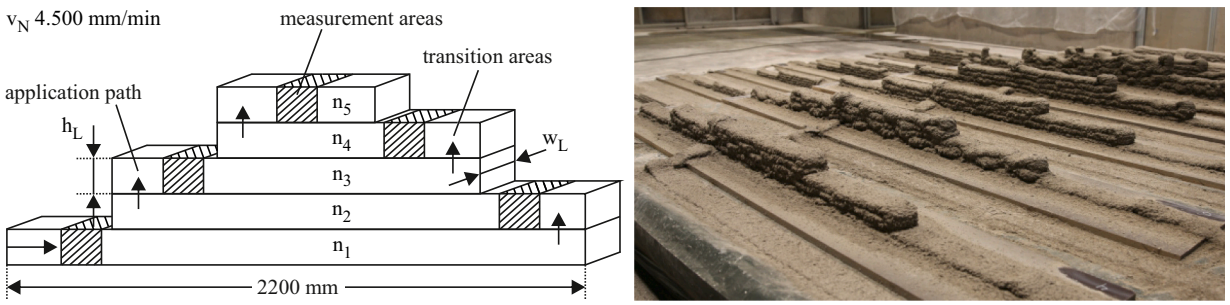

Fig. 3. Pyramidal specimen design with five layers not in scale (left) and 15 printed specimens within the machine working space (right).

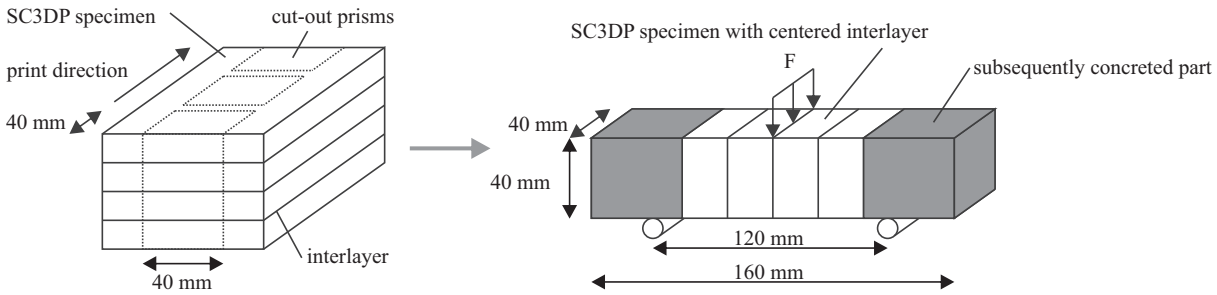

Fig. 4. Principle of sampling for determining the flexural strength (left) and test setup (right).

Fig. 5. 360° endless rotational 2D-Laser-Scanner unit at the robotic end-effector.

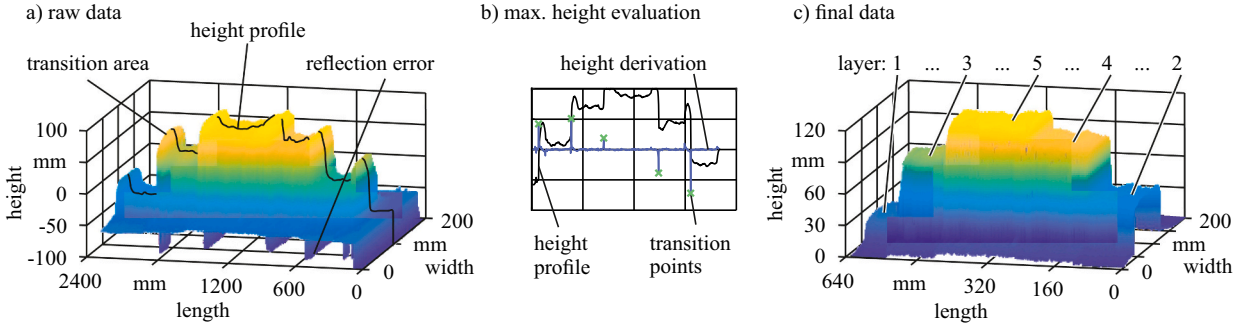

Fig. 6. a) Raw data b) Height evaluation for transition extraction c) Prepared data with deleted transition areas.

the left flank is included while the right one is not. We therefore obtained height evaluation errors up to 5 *mm* when relaying on the mean average. To overcome this inaccuracy we instead choose the median value between the boundaries. According to Fig. 7a), this lead to more precise height values. Fig. 7b) and c) show the usability of the developed evaluation algorithm for the five layers of sample no. $08_{con}3_{acc}40_{air}$ and no. $04_{con}0_{acc}50_{air}$. Since these samples show the most evident geometric differences by visual inspection we assume a correct height and width identification for all other specimens.

2.5. Data reduction and evaluation

Given that only 15 different parameter settings were investigated, the amount of information provided by the scanner data needs to be condensed to 15 matching height and width values before modelling the correlation. To validate a representation by average values, we at first investigate the distribution of the algorithmically determined height and width values for each specimen and layer. Fig. 8 shows histograms of the algorithmically computed width and height values for each recorded cross-sections of the samples with the parameter setting $\dot{v}_{con} = 0.8$. The maximum height and width value from all measurements determine the range of the x axis. The bin size was set to 10 *mm*. Illustrations were sorted in such a way that from the first to the fifth column, the accelerator dosage decreases primarily, and then the air volume flow decreases secondarily.

As can be seen within the top row in Fig. 8, the layers marked by individual color are indistinguishable. Which is reasonable, since the width should not be layer depended and all width data is allocated around a mean value. It must be noted that the width variation can be up to 50 *mm*, but the gaussian distribution indicates a valid representation of the layer width by mean values for further summary. With regard to the height values in the second row, the variation within a layer is significantly lower, whereby the individual layers can be clearly distinguished from each other. It has to be mentioned that sample no. $08_{con}6_{acc}30_{air}$ is showing an anomaly in the first layer. The scattering of the height values over a range of 70 *mm* for this specimen was caused by clogging of the nozzle during the material application. Because of the distribution of the layer height values, a representation by mean average values also appears reasonable, but must be calculated for each layer. Therefore, for further modelling regarding the parameter influence on the layer height and layer width, we resort to the formation of averaged profiles. The resulting mean strand cross-sections are shown in Fig. 9.

The 75 cross-sections need further reduction to match the 15 parameter settings. From the cross-sections, a distinguishable variation

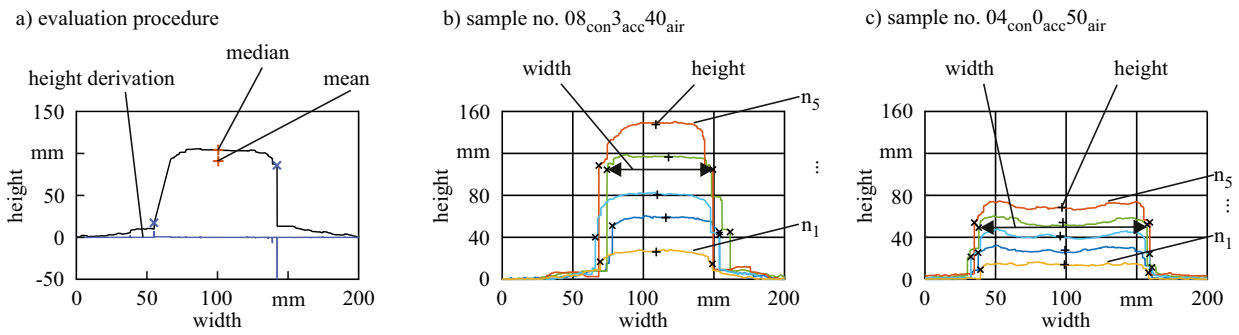

Fig. 7. a) Comparison between average and median evaluation b) Evaluation test with specimen no. $08_{con}3_{acc}40_{air}$ c) Evaluation test with specimen no. $04_{con}0_{acc}50_{air}$.

in the layer surface is evident. While high Dos_{acc} leads to convex shapes in the left half of Fig. 9, printing without accelerator results in concave geometries. Regarding the print path planning and the over all accuracy of the printing process, this behaviour however, only affects the final layer. Therefore we disregard this observation during further investigations.

Based on the average profiles from Fig. 9, we made two assumptions for further condensation of our measurement data. Firstly, the layer width will achieve a stable value for each parameter setting when raising the layer number above a certain amount. Secondly, the overall cross-section height increases approximately linearly with the number of layers, i.e. no significant vertical deformation takes place. Both hypothesis will allow us to calculate a single value for h_L and w_L for each specimen.

To verify our assumptions, we correlate the height and width properties of the averaged cross-section with the layer numbers. Fig. 10a) shows the maximum, median and minimum width for each layer. Maxima and minima are depicted by a horizontal line, while the median is represented by a cross. The maximum width increase between layer one and five can be determined by 5.85 *mm/layer* for sample no. $08_{con}0_{acc}50_{air}$. Regarding an average layer width of 153.67 *mm* for sample no. $08_{con}0_{acc}50_{air}$, the maximum expansion per layer is about 4.05 %. On the opposite side, we can witness a width increase close to zero for sample no. $06_{con}3_{acc}40_{air}$. While a higher layer width increase is assignable to the first layers, the difference is reduced for layer number four and five. The reason for such behaviour can be derived from the stiff wooden surface which the first layer is applied to.

Regarding our assumption of a stable layer width, and to systematically derive a width value that is correlated to the process parameters, we fitted a logarithmic regression through the data sets. The idea is to use the limit of the fitted function as an approximation for the layer width. Those fitted functions are represented by a continuous blue line within Fig. 10a). While we can obtain a stabilization of the layer width within the recorded data, the calculated values from the regression functions are significantly higher than the measured values for the fifth layer. Thus, we decided to use the width values of layer five for further modelling the strand width.

As can be obtained in Fig. 10b), our second assumption of an almost linear correlation between component height and layer number is valid. Here, sample no. $08_{con}6_{acc}30_{air}$ has to be handled with care due to nozzle clogging during the production process. Since the variation of the height values is small and the linear regression fits into the measurement data, the gradient of the linear interpolation is used for further modelling of the layer height. The resulting values for h_L and w_L, used for parametrization of the multi linear regression model, are shown in Table 6.

2.6. Geometric model building and reduction

As first step of calculating the model parameters, we normalised the parameter settings from Table 4 to range from −1 to 1. The transformed model boundaries are given in Table 7. Thereby we obliterate the influences of the varying units towards the model parameters. Calculation of the model parameters was performed using a least-square approach by [34] included in the Matlab fitlm function. Hence the dosage of the accelerator is given in % by weight of cement and in *l/h*, but both have the same physical meaning, only the percentage values were used.

The resulting model constants for h_L, as well as the coefficient specific t- and *p*-values are listed in Table 8. Both values indicate the statistical significance of a coefficient, however, smaller p-values below 0.05 significance level prove the influence of a parameter to a measured result. The t-values have to be outside a dedicated range. We calculated the limits on a significance level of 0.05 and degree of freedom of 10 for the model. The resulting boundaries for the t-values are ±2.31.

The same approach resulted in the parameter values in Table 9, when applied to the layer width values.

The overall evaluation of the models lead to adjusted R-squared values of $R_h = 0.96$ and $R_w = 0.98$ and p-values of $p_h = 0.004$ and $p_w < 0.001$. This at first ensures the quality of the models. However,

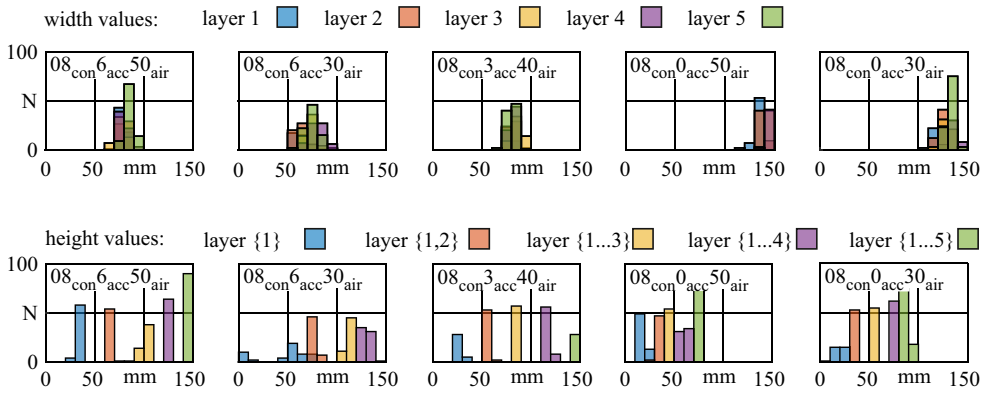

Fig. 8. Histograms of the algorithmically, layer wise computed width and height values with 10 *mm* bins, sample wise shown for $\dot{v}_{con} = 0.8$.

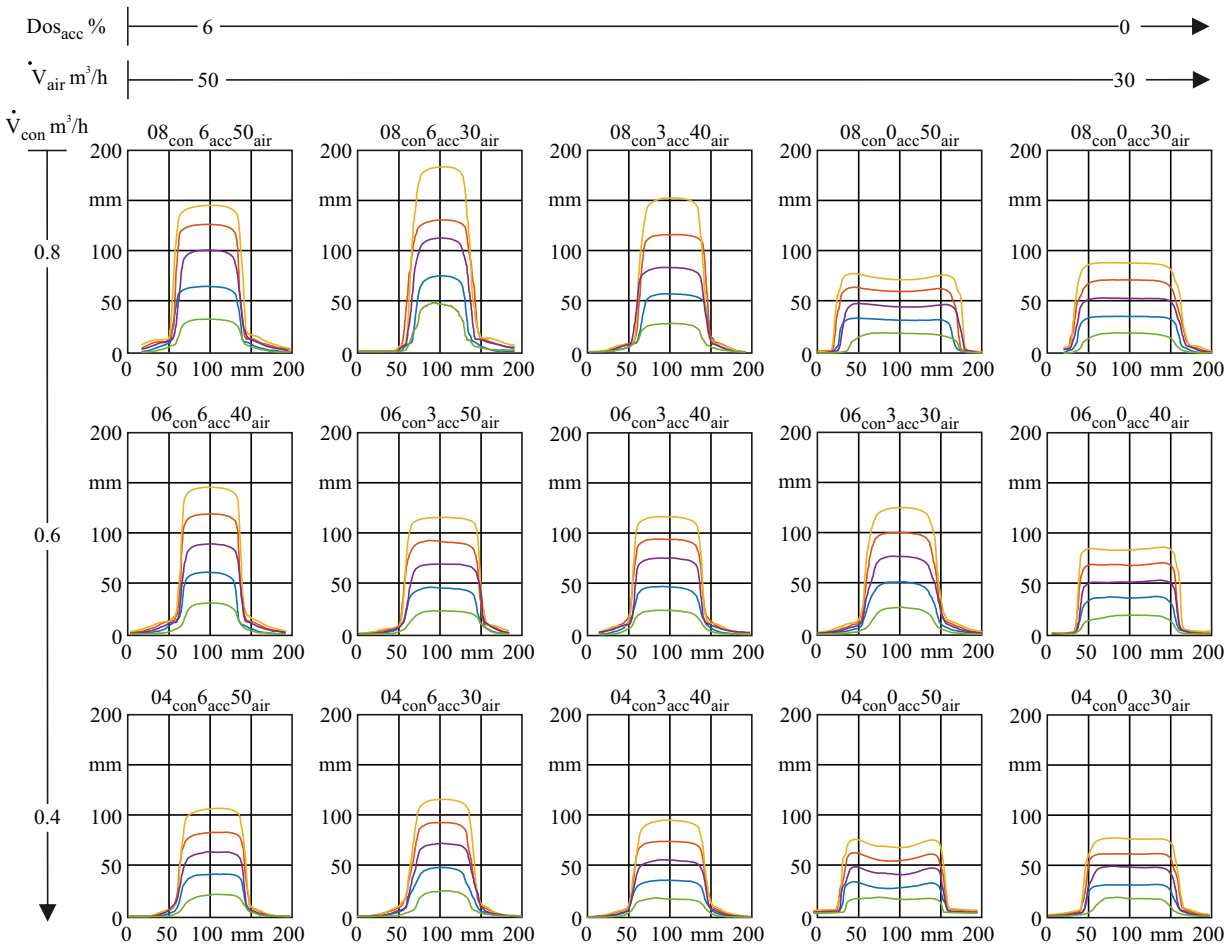

Fig. 9. Averaged strand cross-sections from laser scan profiles.

considering a significance level of 0.05, the p-values only indicate a significant influence on the layer height for $k_{0,\ 2,\ 3}$, and $k_{0,\ 3,\ 6,\ 9}$ regarding the layer width. The t-values provide a similar results.

Both models include non-significant parameters, so reduction of the amount of parameters is sensible. Thereby, we also need less experiments to recalibrate the model in the future. For model reduction, we apply a standard stepwise coefficient elimination and remove in each step the coefficient with the smallest t-value. Minimizing the root-mean-square deviaton (RMSE), which represents the error between modelled and measured data, is used as the stop criterion to maintain the model validity. The RMSE-value for the h_L model is reduced by 15%. The final model results in eq. 5. Within this model, all coefficients except $\dot{v}_{air}^2$ are proven significance by the p- and t-values. The overall p-value for the model is below 0.001 and the adjusted R-squared value is 0.92.

$$\begin{aligned} h_L &= 24.99 \\ &-1.33\dot{v}_{air} + 3.01\dot{v}_{con} + 5.89Dos_{acc} \\ &+1.68\dot{v}_{con}Dos_{acc} \\ &-1.33\dot{v}_{air}^2 - 2.95Dos_{acc}^2 \end{aligned} \tag{5}$$

Performing the same method with the layer width model is reducing the resulting RSME by 12% and leads to eq. 6. Within this model $Dos_{acc}\dot{v}_{air}$ is missing the proven significance. Eliminating this coefficient would result in a similar model as for the layer height, which would seem logical but counteract our systematic evaluation process. As for the height model, the p-value for the width model is also below 0.001 and the adjusted R-squared value is within the same range with 0.96.

$$\begin{aligned} w_L &= 85.31 \\ &+3.66\dot{v}_{air} + 3.73\dot{v}_{con} - 25.81Dos_{acc} \\ &-5.28\dot{v}_{con}Dos_{acc} - 3.33Dos_{acc}\dot{v}_{air} \\ &-6.83\dot{v}_{air}^2 + 14.85Dos_{acc}^2 \end{aligned} \tag{6}$$

It must be noticed that even though the lower model boundary for the concrete volume flow is minus one within the model, the resulting layer height and width is not necessarily zero. However, in the absence of concrete this would be a logical result. Thus, our model is only valid within the investigated model boundaries.

3. Results of model adoption and validation

For an initial validation, the model prediction results can be compared with the measurements. Therefore, Fig. 11 shows the model prediction values in comparison to the measurement values. Beside the red circular mean measurement values, also the maximum and minimum of the height and width for each specimen is displayed by a red horizontal line. It can be derived that the average mean error of the height model is as low as 4.41%, which is about 0.9 *mm* of deviation for a single layer. However, it must be considered that a maximum deviation of 11.05% for the prediction is possible. Detailed examination of the width prediction provides similar prediction accuracy. The maximum deviation is at 8.3% and the average error is 2.8%. While this specifically shows the capability of the reduced model to represent the measured values, additional validation experiments are required to confirm the selected correlations. Therefore, we performed seven additional tests. We choose the first test setting of the validation according to the initial

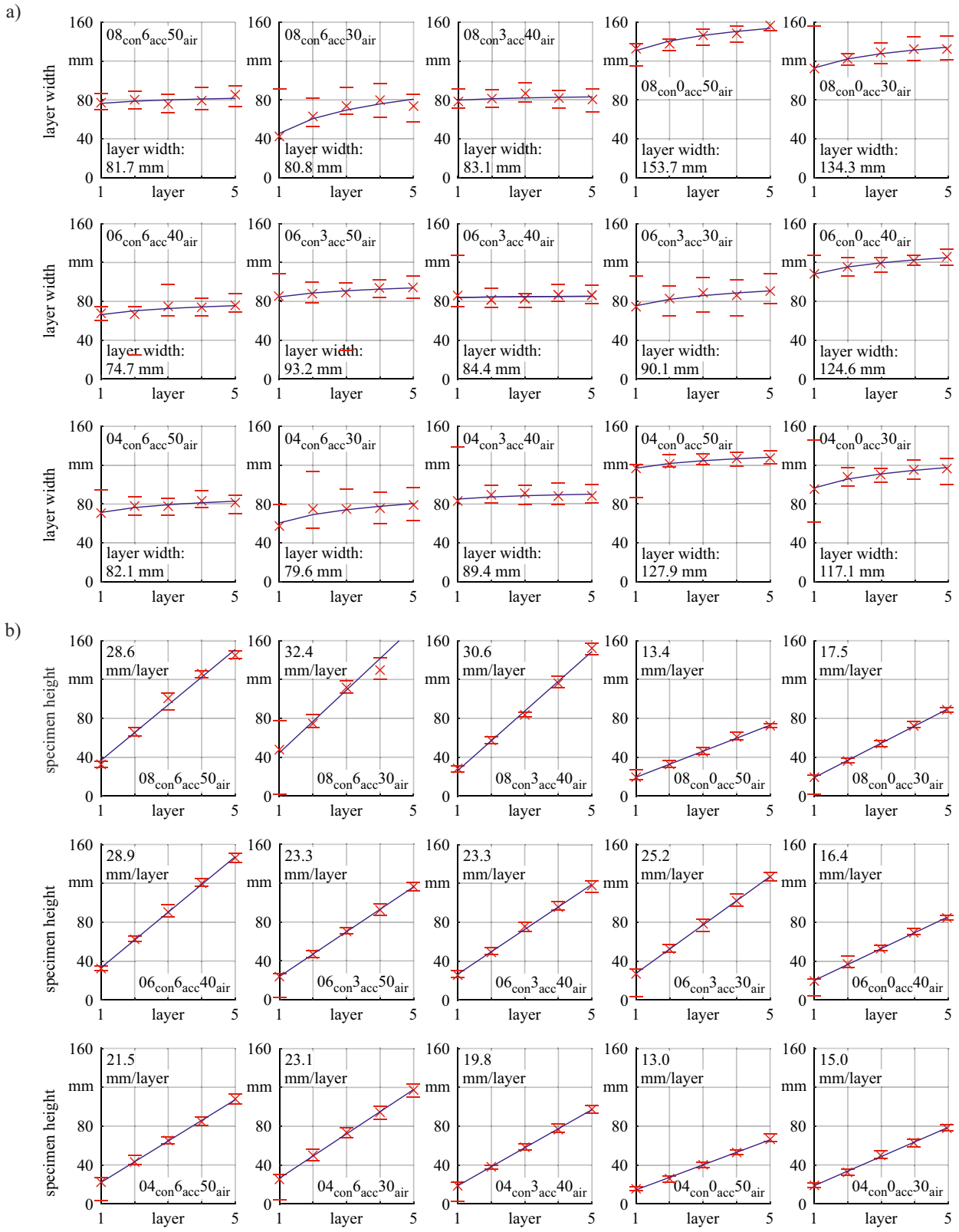

Fig. 10. Maximum (–), median(x) and minimum (–) a) Width and b) Cumulated height values for each layer.

model center point $\dot{v}_{con}$ 0.6 *m/h*, Dos_{acc} 3 % and $\dot{v}_{air}$ 40 *m/h*. Since we expect environmental influences to slightly change the material properties compared to our first experiments, we use the repetition of the center point to adapt the k_0 values for the height and width model. This proceeding also met our requirement to provide an easily adaptable model. The measured height and width values for the repetition of setting $0.6_{con}3_{acc}40_{air}$ are given in Table 10 and compared to the first experiment to determine the correction values for the adapted $k_{0,\,h,\,a}$ and $k_{0,\,w,\,a}$.

Six additional parameter settings were chosen in circular manner

Table 6
Condensed values for h_L and w_L.

No.	h_L [mm]	w_L [mm]
$08_{con}6_{acc}50_{air}$	28.55	81.66
$08_{con}6_{acc}30_{air}$	32.36	80.76
$08_{con}3_{acc}40_{air}$	30.64	83.12
$08_{con}0_{acc}50_{air}$	13.42	153.67
$08_{con}0_{acc}30_{air}$	17.52	134.26
$06_{con}6_{acc}40_{air}$	28.87	74.66
$06_{con}3_{acc}50_{air}$	23.32	93.15
$06_{con}3_{acc}40_{air}$	23.33	84.43
$06_{con}3_{acc}30_{air}$	25.20	90.08
$06_{con}0_{acc}40_{air}$	16.40	124.61
$04_{con}6_{acc}50_{air}$	21.51	82.13
$04_{con}6_{acc}30_{air}$	23.07	75.59
$04_{con}3_{acc}40_{air}$	19.79	89.44
$04_{con}0_{acc}50_{air}$	13.04	127.86
$04_{con}0_{acc}30_{air}$	15.00	117.12

Table 7
Normalised volume flow input parameters [−1;1].

	$min._{real}$	$max._{real}$	$min._{model}$	$max._{model}$
$\dot{v}_{con}$	0.4	0.8	−1	1
Dos_{acc}	0	6	−1	1
$\dot{v}_{air}$	30	50	−1	1

around the initial center point setting. The settings are chosen to lay within the design of experiments which we used for model building. Fig. 12 shows the validation points within the original modelling space.

Table 11 contains the parameter settings as *no*. as well as the measured width and height values w_L and h_L, the model predictions mod. $_w$ and mod.$_h$ of the adapted model, and the resulting error values. Since the variation within the modelled and the measured height and width values is only about ±15%, proving the significance of the prediction model is necessary.

In this regard, we at first used the MATLAB function *corrcoef*, based on the approach given by [35], to calculate the correlation between each combination of measured and predicted value. With 0.81 for the width values and 0.93 for the height values both results are close to 1 and indicate a strong dependency between model and test data. The correlating R2 of $R2_h$ 0.65 and $R2_w$ 0.78 further support the assumption of trustworthy predictability through the adjusted multi-linear regression. Based on the statistical validity, adjusting the constant coefficients to $k_{0, ..., a}$ leads to a maximum width deviation of −8 % and a maximum height prediction error of +7.5 %. The mean values are at 5 % for w_L and 4 % regarding h_L, and therefore similar to our initial model.

4. Discussion of parameter influences and model results

Based on the validation of the proposed model, in this section we will discuss the observable adjustabillity of the model and the strand properties, as well as the influence of the investigated parameters on the interlayer bond strength.

4.1. Strand geometry

Given the R-squared values resulting from fitting our reduced multi-linear regression into the obtained process results, it can be stated that the model is capable of describing the correlations. In combination with the successful model adjustment through solely changing the constant offsets $k_{0, ...}$ to $k_{0, ..., a}$, we can further assume general applicability of the selected influencing parameters and the remaining calculated weights $k_{1, ..., 9}$. Based on this assumption, we can use the behaviour of the model and the depicted influences of the printing parameters, to determine the adaptability of the path geometry.

Considering the results in eq. (5) and (6), a linear or even quadratic

Table 8
Linear regression coefficients for h_L with normalised volume flow input parameters [−1;1].

h_L	coefficient		t-values	p-values
k_0	25.07	const.	23.61	< 0.001
k_1	−1.33	$\dot{v}_{air}$	−2.12	0.087
k_2	3.01	$\dot{v}_{con}$	4.81	0.005
k_3	5.90	Dos_{acc}	9.44	< 0.001
k_4	−0.54	$\dot{v}_{air}\dot{v}_{con}$	−0.78	0.468
k_5	0.09	$\dot{v}_{air}Dos_{acc}$	0.12	0.905
k_6	1.68	$\dot{v}_{con}Dos_{acc}$	2.40	0.061
k_7	−1.24	$\dot{v}_{air}2$	−1.01	0.36
k_8	−0.29	$\dot{v}_{con}2$	−0.24	0.82
k_9	−2.87	$Dos_{acc}2$	−2.32	0.07

Table 9
Linear regression coefficients for w_L with normalised volume flow input parameters [−1;1].

w_L	coefficient		t-values	p-values
k_0	84.98	const.	29.27	< 0.001
k_1	3.66	$\dot{v}_{air}$	2.15	0.08
k_2	3.73	$\dot{v}_{con}$	2.19	0.08
k_3	−25.87	Dos_{acc}	−15.15	< 0.001
k_4	0.87	$\dot{v}_{air}\dot{v}_{con}$	0.46	0.66
k_5	−3.33	$\dot{v}_{air}Dos_{acc}$	−1.74	0.14
k_6	5.28	$\dot{v}_{con}Dos_{acc}$	−2.76	0.03
k_7	6.50	$\dot{v}_{air}2$	1.93	0.11
k_8	1.16	$\dot{v}_{con}2$	0.34	0.75
k_9	14.52	$Dos_{acc}2$	4.31	< 0.007

influence of the air volume flow, as well as of the accelerator dosage is indicated. Furthermore, the correlation between the concrete volume flow and the accelerator dosage is non-neglectable. While all other two-factor correlations have shown no significant influence on the layer height, the combination of the accelerator dosage and air flow is changing the layer width. As expected all single terms must also be included within the model. For an improved investigation, Fig. 13 shows the model surfaces for our three accelerator settings and the initially generated model.

From Fig. 13 a) it can be concluded that the accelerator dosage Dos_{acc} has the highest influence to the layer height, which is understandable as the material's yield stress and stiffness is significantly increased [16] in line with the modulus of deformation. It can also be observed that the range of adjustable layer heights is increased by the accelerator. For an accelerator content of 0% the deviation between the minimal and maximal layer height is at 5 *mm*, while for 6% we can achieve a range of 10 *mm*. The opposite behaviour appears for the development of the layer width as is shown in 13 b). Not only does the accelerator significantly reduce the layer width but also decreases the adjustability. Detailed ranges for h_L and w_L related to the accelerator dosage are listed in Table 12.

A less distinctive influence on the layer width is determined by the concrete volume flow $\dot{v}_{con}$. For low accelerator rates, increasing the amount of concrete will mainly raise the layer width based on volume constancy and affected by intensified flow through enhanced shear rate. The influence of the accelerator, however, will change the impact of the concrete volume flow rate. Based on the 3% and 6% investigations and the model, the material will mostly build up in a vertical direction while only minor changes in the layer width are obtained.

The least variability is provided by the air volume flow $\dot{v}_{air}$. When closely investigating Fig. 13 a), it can be obtained that the layer height will increase only about 3 *mm* for each given accelerator and concrete flow rate, when $\dot{v}_{air}$ is reduced. This heightening is correlated with a layer width reduction by 20 *mm*, observable in Fig. 13 b), for low accelerator dosages. For up to 6% Dos_{acc}, the width variety is down to 5 *mm*. Both observations are explainable by widening of the strand due to the increased air volume flow, and the higher impact velocity.

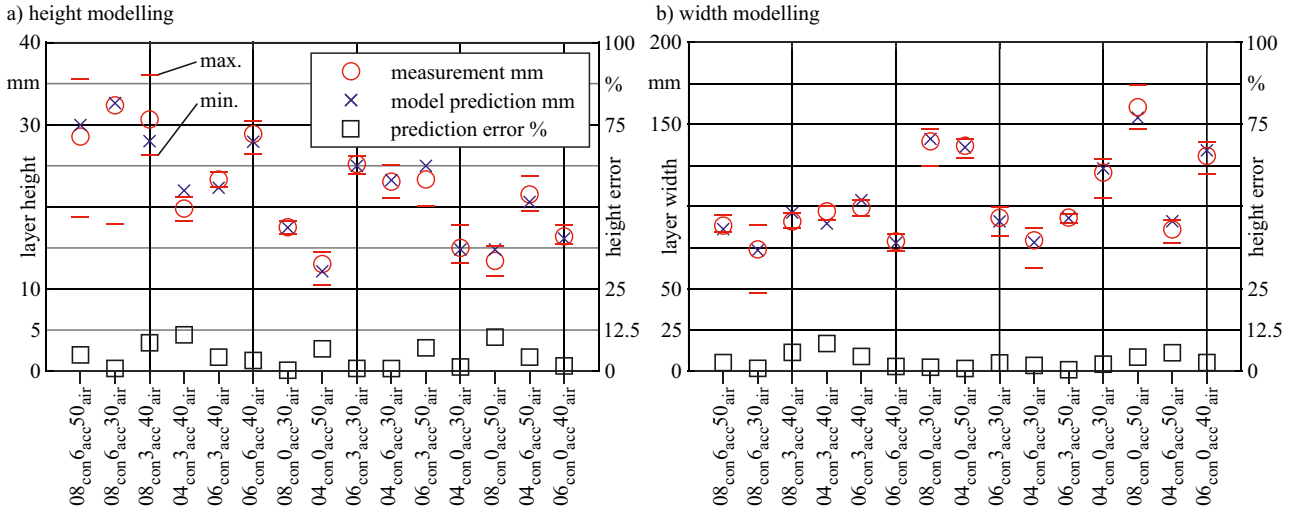

Fig. 11. Comparisson between the model values and the average, maximum and minimum measurement values for the layer height a) and width b).

Table 10
Correction values for $k_{0, \ldots, a}$ based on the center point repetition.

	w_L [mm]	h_L [mm]
Initial measured values	85.3	24.9
Repeated measured values	97.6	23.7
Adapted $k_{0,\ldots,a}$	$k_{0,w} + 12.3$	$k_{0,h}$-1.2

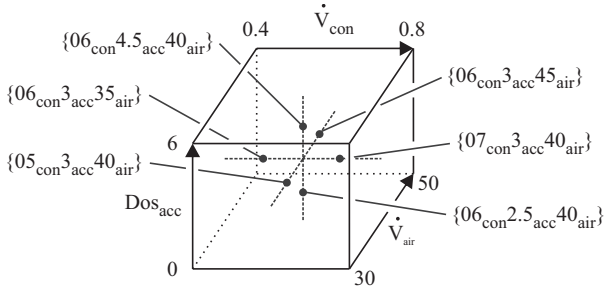

Fig. 12. Parameter settings for model validation.

Table 11
Condensed values for h_L and w_L in comparison to the prediction by the updated model with adapted $k_{0, \ldots, a}$ for the validation experiments.

No.	w_L [mm]	mod.$_w$ [mm]	error [%]	h_L [mm]	mod.$_h$ [mm]	error [%]
$06_{con}3_{acc}35_{air}$	98.0	94.1	−3.90	23.2	24.1	3.88
$06_{con}2.5_{acc}40_{air}$	112.7	114.2	1.33	20.5	20.1	−2.57
$05_{con}3_{acc}40_{air}$	104.1	95.7	−8.09	21.1	22.2	5.89
$06_{con}3_{acc}45_{air}$	103.2	97.7	5.33	21.2	22.8	7.54
$06_{con}4.5_{acc}40_{air}$	84.4	88.4	4.75	27.1	26.0	4.06
$07_{con}3_{acc}40_{air}$	93.1	99.4	6.76	25.5	25.3	0.78

Correlating the observations of the model evaluation with the measured values given in Table 12, we can state that the adjustability of the layer height can be maximized through increased accelerator dosage, while the layer width is more flexible without accelerator. For moderate accelerator dosages the width can be adjusted by tuning the air flow, while the layer height is more responsive to the concrete flow.

Concerning the parameter ranges, nozzle clogging occurred during setting $08_{con}6_{acc}30_{air}$. Therefore, the resulting cross-sections are neither equidistant nor of constant width. While no actual clogging appeared for all other accelerator volume flow settings at 6 %, we obtained indicators for an inconsistent material output. Thus, we state a process limit when raising accelerator volume flow rates above 6 %.

4.2. Interlayer bond strength

In order to investigate the effect of variations in material and process parameters on the interlayer bond strength, the flexural strength with a load parallel to the layer orientation was determined on the SC3DP specimens. The test was performed by a 3-point bending test (compare section 2.3.4).

Fig. 14 a) shows the flexural strength as a function of accelerator dosage Dos_{acc} (0, 3, and 6 % bwoc) under a constant concrete volume flow $\dot{v}_{con}$ (0.8 m^3/h) and for varying air volume flows $\dot{v}_{air}$ of 30 m^3/h (diamonds), 40 m^3/h (square) 50 m^3/h (circles). Fig. 14 b) shows the dependence of the flexural strength on the air volume flow $\dot{v}_{air}$ (30, 40 and 50 m^3/h) at a constant accelerator dosage Dos_{acc} (6 % bwoc) and for different concrete volume flows $\dot{v}_{con}$ of 0.4 m^3/h (black line), 0.6 m^3/h (square) and 0.8 m^3/h (light grey line). Three samples were evaluated for each parameter setting. Due to the exclusion criterion of not considering samples that did not fail in the middle third, only two samples were evaluated for the process parameter combination $08_{con}6_{acc}30_{air}$. The flexural strength over all parameter variations ranges from 4.3 to 8.7 N/mm^2, which is in line with existing results on SC3DP specimens [16].

Fig. 14a shows that the accelerator dosage has a great influence on the flexural strength. The flexural strength decreases with increasing accelerator dosage. This is mainly attributed to an increase in static yield stress as well as a high structural build-up of the fresh concrete, as the interface tortuosity, i.e. the interlocking between the layers, is decreasing with increasing yield stress [16,26,36]. In addition, the flexural strength also decreases due to increasing air inclusions in the interlayer zone with increasing Dos_{acc} [22,36].

Besides the accelerator dosage, the air volume flow has an influence on the flexural strength, see Fig. 14b. We observed that increasing the air volume flow results in an increase in flexural strength. This can be attributed to the increasing kinetic energy of the sprayed material at higher air volume flows [16,26,36]. The higher kinetic energy leads to a higher interface tortuosity and therefore a better interlocking between the layers. Furthermore, increasing compaction of the concrete at higher air volume flows plays a role. We found that an increase in air volume flow rate is accompanied by an increase in the density of the sprayed material, from 1.97 g/cm^3 at 30 m^3/h to 2.09 g/cm^3 at 50 m^3/h (Dos_{acc} = 6 %, $\dot{v}_{con}$ = 0.8 m^3/h), [36].

While the concrete volume flow shows a large influence on the ge-

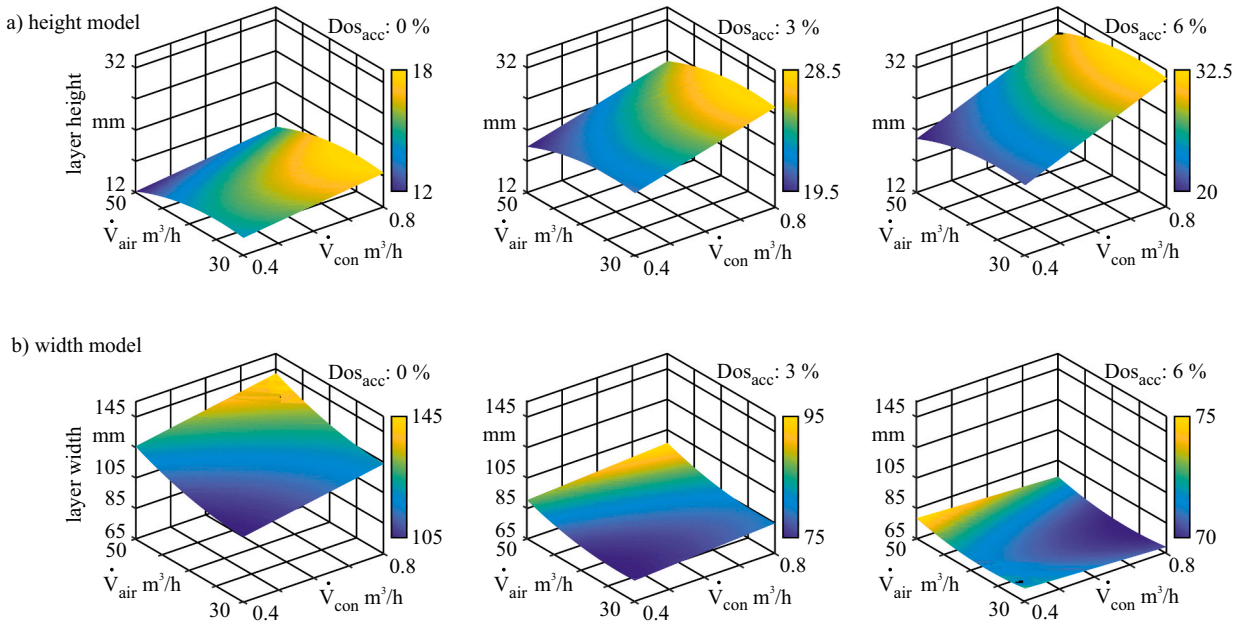

Fig. 13. Model based calculation of a) layer height and b) width for the three investigated accelerator dosages of 0, 3 and 6% and the unadapted model.

Table 12
Geometric boundaries according to accelerator content.

	w_L [mm]	h_L [mm]
%	109–144 ± 14%	13–18 ± 14%
%	82–90 ± 5%	20–31 ± 22%
%	67–80 ± 9%	22–32 ± 20%

ometry of the applied strands (cf. capter 9.1), it only shows an effect on the flexural strength for low air volume flow rates (Fig. 14b)). For a high air volume flow, equal flexural strengths are obtained. This could be attributed to the fact that for an air volume flow of $\dot{v}_{air} = 50\ m^3/h$, maximum compaction is achieved regardless of the concrete volume flow used here.

The results show that the variation of process and material parameters not only affects the strand geometry but also the hardened state properties, i.e. the interlayer bond strength. For the investigated range of these three parameters, especially the accelerator dosage and air volume flow show a pronounced effect on hardened state properties. In principle, the process parameters can be changed independently of each other during the printing process. However, when changing several parameters at the same time, it should be considered that there is a pronounced interaction between the parameters with regard to the mechanical properties. For example, while a variation of the concrete volume flow at high air volume flows shows no significant effect on the flexural strength, a reduction of the flexural strength results with increasing concrete volume flow at low air volume flow rates, see Fig. 14b). Since the hardened state properties are of particular importance for the manufacturing of structural components, it is necessary to consider the previously mentioned material-process-interaction. Thus, the required hardened state properties have to be implemented as control limits in addition to a purely geometrically focused path planning procedure. Depending on the mechanical requirements of the planned structure, it is recommended to choose the material and process parameters accordingly. For example for high mechanical performance and high strand heights, it may be useful to limit the amount of used

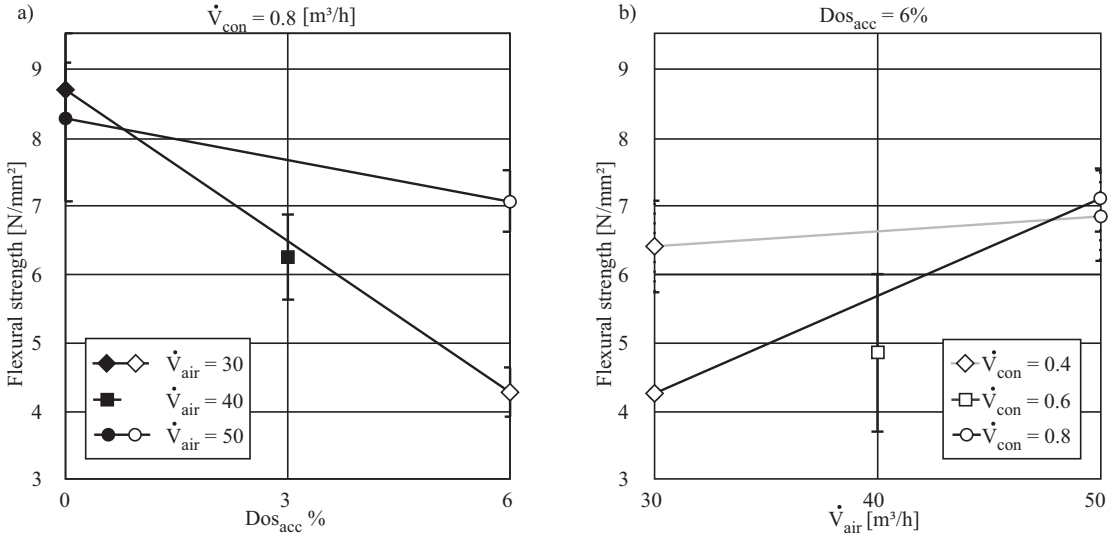

Fig. 14. 28 d flexural strength of SC3DP-specimen as a function of (a) the accelerator dosage as well as (b) the air volume flow.

accelerator and use higher concrete and air volume flows instead.

4.3. Mock-up

Given the known correlations between the process and material parameters and the process result, we used the adapted model to determine the printing parameters for a mock -up. The test wall was designed with a length of 1.600 *mm*, a layer width of 120 *mm* and a layer height of 15 *mm*. Since the accelerator dosage is increasing the risk of nozzle clogging, it is only used in case of stability concerns, and thus not required for the sample component resulting in Dos_{acc} at 0 %. The desired layer height and layer width are subject to both of the remaining parameters $\dot{v}_{con}$ and $\dot{v}_{air}$, we decided to tune them according to their sensitivity. We first adjusted the modelled layer height by setting $\dot{v}_{con}$ to 0.62 m^3/h and keeping $\dot{v}_{air}$ at 40 m^3/h. In the second step, we levelled $\dot{v}_{air}$ at 29.0 m^3/h to achieve the desired layer width within our model. To ensure similar rheological behaviour we utilized the same material mixture and processing as for the model building experiments. Furthermore the flow table test indicated comparable values with f = 45 *cm* ± 1.1 *cm*.

Fig. 15 shows the final component and the correlated 3D scan. The 3D scanning is conducted to evaluate the final component accuracy. The produced layer width, was measured by the distance from the left to the right side of the point cloud and is about 121 *mm* and deviates about 0.8% from the desired value. Regarding the layer height values the deviation between the targeted component height of 450 *mm* and the produced part is −56 *mm*. This height loss can be transferred to −1.8 *mm* per layer and results in a deviation of 12 %. While this value is higher than the expected error, it is necessary to consider the load dependent plastic deformation of the printed concrete. In this regard, the material will compact itself which cannot be predicted in full scale based on the initially investigated five layers. Based on the precise prediction of the width, it can be assumed that we are capable of precisely estimating the resulting layer geometry, but the compaction and spray shadow reduce the amount of applied material for lager printing processes and thus reduce the resulting height.

5. Conclusion

Shotcrete 3D Printing is subject to varying strand geometries throughout day-to-day printing, caused by irregular environmental characteristics as well as by fluctuations in the mix composition, e.g. as a result of different material batches. Thus, setting constant process parameters correlated to fixed print path planning values for multiple printing operations results in a vast deviation between designated and printed geometry. To ensure improved printing accuracy and higher process control, we aimed for a process adjustment based on a tunable modelling approach within reasonable process limits.

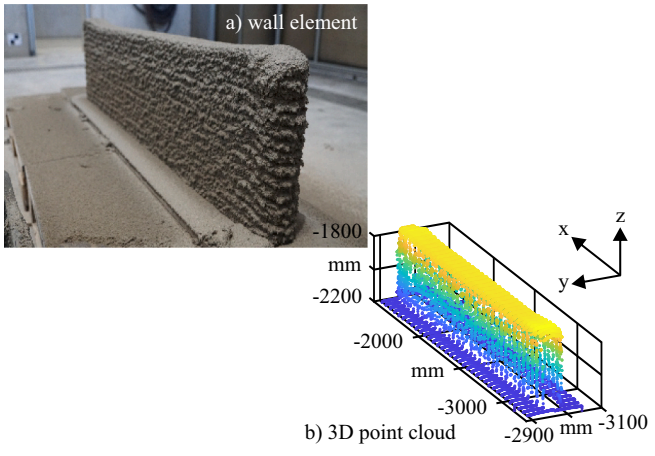

Fig. 15. a) Printed sample wall with process parameters set according to the adapted model to achieve planed layer height and width b) 3D scanned point cloud for geometrical evaluation.

For this purpose, we have carried out experimental investigations showing the influence of material and process parameters (accelerator dosage, air volume flow and concrete volume flow) on the resulting strand geometry. To evaluate the adjustability of the strand properties, we then built a multi-linear regression model based on our investigations. This model shows a clear positive influence of Dos_{acc} on the strand height, while a reduced strand width is observed. Furthermore, we found that reducing $\dot{v}_{con}$ can be used to counteract the height increase and that adjusting $\dot{v}_{air}$ is an option to tune the layer width. Within the investigated process limits, results show an adjustability of the path width from 75 to 154 *mm* and of the height from 13 to 32 *mm*. However, the model parameters show a significant influence of coupled effects, which means that a combined consideration of the parameters is necessary in any case.

Since the hardened state properties are of particular importance for the manufacturing of structural components, we have additionally investigated the influence of the material and process parameters on the mechanical properties, i.e. interlayer bond strength, of the manufactured specimens. It could be observed that an increasing accelerator dosage was accompanied by a reduction of the interlayer bond strength. This influence on the interlayer bond thus limits the range of the accelerator dosage for controlling the component geometry. However, by increasing the air volume flow, an improvement of the interlayer bond strength was achieved, resulting in a counteraction of the negative effect of the accelerator.

Through combination of the proposed measurement system and the evaluation algorithms, adjusting the shotcrete strand properties by tuning the material and process parameters is possible. It must be said that at least one experiment is required to recalibrate the model. In this regard, our validation process proves that a decent prediction capability can be assured by repetition of the center point. Based on the validation data the adapted model was used for the path planning and production of the 1.600 by 450 *mm* sample wall. However, for the 450 *mm* high wall element we obtained a deviation of −50 *mm* between the desired and the final component height. The reason for this behaviour can be found in the fact that our model does not take into account any load based material deformation or irregularities within the material supply during the printing process.

6. Outlook

The proposed modelling approach provides a sufficient estimation of the initial layer geometry. However, manufacturing of larger components will require an additional control algorithm to adjust the printing parameters during production. Especially for large-scale manufacturing a feedback process control is necessary to counteract load induced deformations and the instability of spray processes. Therefore, we want to use the developed scanning unit to monitor our production process and generate real-time information. The preplanned path geometry will serve as set point and will supply values, which can be compared to our in-process measurement. Using the proposed model and additionally take into account the spray distance and nozzle feed rate we will be able to compensate for the layer height and width deviations. First results to control the process based on an initial strand estimation with the proposed model are described in [37]. At this point we need to make clear, that we have only presented investigations of three of the process parameters, however to fully control the SC3DP, the influence of the collectivity of parameters, including level one and three, must be investigated.

Furthermore, the presented results of the mechanical tests clearly showed that the material and process parameters used for process control affect the resulting hardened concrete properties. In general, the interlayer bond strength should be assessed individually based on the

required component quality, so that finally limitations of the process control variables can be defined.

Declaration of Competing Interest

The authors declare that they have no known competing financial interests or personal relationships that could have appeared to influence the work reported in this paper.

Data availability

Data will be made available on request.

Acknowledgements

The authors gratefully acknowledge the funding by the Deutsche Forschungsgemeinschaft (DFG – German Research Foundation) – Project no. 414265976. The authors would like to thank the DFG for the support within the SFB/Transregio 277 – Additive manufacturing in construction. (Subproject B04 and A04).

References

[1] H. Karimi, T.R. Taylor, P.M. Goodrum, Analysis of the impact of craft labour availability on north american construction project productivity and schedule performance, Constr. Manag. Econ. 35 (6) (2017) 368–380, https://doi.org/10.1080/01446193.2017.1294257.
[2] R. Bogue, What are the prospects for robots in the construction industry? Industrial Robot: Int. J. (2018) https://doi.org/10.1108/IR-11-2017-0194.
[3] O. Babalola, E.O. Ibem, I.C. Ezema, Implementation of lean practices in the construction industry: a systematic review, Build. Environ. 148 (2019) 34–43, https://doi.org/10.1016/j.buildenv.2018.10.051.
[4] N. Melenbrink, J. Werfel, A. Menges, On-site autonomous construction robots: towards unsupervised building, Autom. Constr. 119 (2020), 103312, https://doi.org/10.1016/j.autcon.2020.103312.
[5] K.H. Petersen, N. Napp, R. Stuart-Smith, D. Rus, M. Kovac, A review of collective robotic construction, Sci. Robot. 4 (28) (2019), https://doi.org/10.1126/sciadv.abk0685.
[6] W.S. Alaloul, M. Liew, N.A.W.A. Zawawi, I.B. Kennedy, Industrial revolution 4.0 in the construction industry: challenges and opportunities for stakeholders, Ain Shams Eng. J. 11 (1) (2020) 225–230, https://doi.org/10.1016/j.asej.2019.08.010.
[7] R. Maskuriy, A. Selamat, P. Maresova, O. Krejcar, O.O. David, Industry 4.0 for the construction industry: review of management perspective, Economies 7 (3) (2019) 68, https://doi.org/10.3390/economies7030068.
[8] C. Beyer, Strategic implications of current trends in additive manufacturing, J. Manuf. Sci. Eng. 136 (6) (2014), https://doi.org/10.1115/1.4028599.
[9] A. Perrot, 3D Printing of Concrete: State of the Art and Challenges of the Digital Construction Revolution, John Wiley & Sons, 2019. ISBN:978–1–786-30341-7.
[10] F. Brun, F. Gaspar, A. Mateus, J. Vitorino, F. Diz, Experimental Study on 3d Printing of Concrete with Overhangs, 2020, pp. 778–789, https://doi.org/10.1007/978-3-030-49916-7-77.
[11] J. Jiang, J. Stringer, X. Xu, R.Y. Zhong, Investigation of printable threshold overhang angle in extrusion-based additive manufacturing for reducing support waste, Int. J. Comput. Integr. Manuf. 31 (10) (2018) 961–969, https://doi.org/10.1080/0951192X.2018.1466398.
[12] B. Zareiyan, B. Khoshnevis, Effects of interlocking on interlayer adhesion and strength of structures in 3d printing of concrete, Autom. Constr. 83 (2017) 212–221, https://doi.org/10.1016/j.autcon.2017.08.019.
[13] E. Hosseini, M. Zakertabrizi, A.H. Korayem, G. Xu, A novel method to enhance the interlayer bonding of 3d printing concrete: an experimental and computational investigation, Cem. Concr. Compos. 99 (2019) 112–119, https://doi.org/10.1016/j.cemconcomp.2019.03.008.
[14] V.N. Nerella, S. Hempel, V. Mechtcherine, Effects of layer-interface properties on mechanical performance of concrete elements produced by extrusion-based 3d-printing, Constr. Build. Mater. 205 (2019) 586–601, https://doi.org/10.1016/j.conbuildmat.2019.01.235.
[15] E. Keita, H. Bessaies-Bey, W. Zuo, P. Belin, N. Roussel, Weak bond strength between successive layers in extrusion-based additive manufacturing: measurement and physical origin, Cem. Concr. Res. 123 (2019), 105787, https://doi.org/10.1016/j.cemconres.2019.105787.
[16] I. Dressler, N. Freund, D. Lowke, The effect of accelerator dosage on fresh concrete properties and on interlayer strength in Shotcrete 3d Printing, Materials 13 (2) (2020) 374, https://doi.org/10.3390/ma13020374.
[17] H. Lindemann, R. Gerbers, S. Ibrahim, F. Dietrich, E. Herrmann, K. Dröder, A. Raatz, H. Kloft, Development of a Shotcrete 3d-Printing (sc3dp) technology for additive manufacturing of reinforced freeform concrete structures, in: RILEM International Conference on Concrete and Digital Fabrication, Springer, 2018, pp. 287–298.
[18] N. Hack, H. Kloft, Shotcrete 3d Printing technology for the fabrication of slender fully reinforced freeform concrete elements with high surface quality: A real-scale demonstrator, in: RILEM International Conference on Concrete and Digital Fabrication, Springer, 2020, pp. 1128–1137.
[19] B. Lu, Y. Qian, M. Li, Y. Weng, K.F. Leong, M.J. Tan, S. Qian, Designing spray-based 3d printable cementitious materials with fly ash cenosphere and air entraining agent, Constr. Build. Mater. 211 (2019) 1073–1084, https://doi.org/10.1016/j.conbuildmat.2019.03.186.
[20] L. Lachmayer, R. Dörrie, H. Kloft, A. Raatz, Automated Shotcrete 3d Printing-printing Interruption for Extended Component Complexity, XXX, 2021.
[21] S. Neudecker, C. Bruns, R. Gerbers, J. Heyn, F. Dietrich, K. Dröder, A. Raatz, H. Kloft, A new robotic spray technology for generative manufacturing of complex concrete structures without formwork, Procedia CIRP 43 (2016) 333–338, https://doi.org/10.1016/j.procir.2016.02.107.
[22] H. Kloft, H.-W. Krauss, N. Hack, E. Herrmann, S. Neudecker, P.A. Varady, D. Lowke, Influence of process parameters on the interlayer bond strength of concrete elements additive manufactured by Shotcrete 3d Printing (sc3dp), Cem. Concr. Res. 134 (2020), 106078, https://doi.org/10.1016/j.cemconres.2020.106078.
[23] R.A. Buswell, W.L. da Silva, F.P. Bos, H. Schipper, D. Lowke, N. Hack, H. Kloft, V. Mechtcherine, T. Wangler, N. Roussel, A process classification framework for defining and describing digital fabrication with concrete, Cem. Concr. Res. 134 (2020), 106068, https://doi.org/10.1016/j.cemconres.2020.106068.
[24] R. Dörrie, H. Kloft, Force flow compliant robotic path planning approach for reinforced concrete elements using sc3dp, in: Third RILEM International Conference on Concrete and Digital Fabrication, Springer International Publishing, 2022, pp. 370–375, https://doi.org/10.1007/978-3-031-06116-5-55.
[25] S. Ibrahim, A. Olbrich, H. Lindemann, R. Gerbers, H. Kloft, K. Dröder, A. Raatz, Automated additive manufacturing of concrete structures without formwork-concept for path planning, in: Tagungsband des 3. Kongresses Montage Handhabung Industrieroboter, Springer, 2018, pp. 83–91, https://doi.org/10.1007/978-3-662-56714-2-10.
[26] I. Dressler, N. Freund, D. Lowke, Control of strand properties produced with Shotcrete 3d Printing by accelerator dosage and process parameters, in: RILEM International Conference on Concrete and Digital Fabrication, Springer, 2020, pp. 42–52.
[27] L. Lachmayer, V. Ekanayaka, A. Hürkamp, A. Raatz, Approach to an optimized printing path for additive manufacturing in construction utilizing fem modeling, Procedia CIRP 104 (2021) 600–605, https://doi.org/10.1016/j.procir.2021.11.101.
[28] S. Moser, G. Girmscheid, Fully automated shotcrete robot, in: RILEM International Conference on Concrete and Digital Fabrication, 1999, pp. 358–390. http://pascal-francis.inist.fr/vibad/index.php?action=getRecordDetailidt=1538615.
[29] G. Girmscheid, S. Moser, Fully automated shotcrete robot for rock support, Computer-aided Civil Infrastructure Eng. 16 (2001) 200–215, https://doi.org/10.1111/0885-9507.00226.
[30] N. Ginouse, M. Jolin, Investigation of spray pattern in shotcrete applications, Constr. Build. Mater. 93 (2015) 966–972, https://doi.org/10.1016/j.conbuildmat.2015.05.061.
[31] B. Schuler, O. Sawodny, Spray pattern analysis using wet-mix concrete for model based process control towards automated construction, in: In: 2019 IEEE 15th International Conference on Automation Science and Engineering (CASE), IEEE, 2019, pp. 661–666, https://doi.org/10.1109/COASE.2019.8842853.
[32] B. Lu, M. Li, T.N. Wong, S. Qian, Effect of printing parameters on material distribution in spray-based 3d concrete printing (s-3dcp), Autom. Constr. 124 (2021), 103570, https://doi.org/10.1016/j.autcon.2021.103570.
[33] A.B. Eldin, General introduction to design of experiments (doe), in: Wide Spectra of Quality Control 2, 2011, pp. 21–26, https://doi.org/10.5772/23878.
[34] P.W. Holland, R.E. Welsch, Robust regression using iteratively reweighted least-squares, Commun. Stat. Theory Methods 6 (9) (1977) 813–827, https://doi.org/10.1080/03610927708827533.
[35] R.A. Fisher, Statistical Methods for Research Workers, 1992, pp. 66–70, https://doi.org/10.1007/978-1-4612-4380-9-6.
[36] D. Böhler, I. Mai, N. Freund, L. Lachmayer, A. Raatz, D. Lowke, Influence of material and process parameters on hardened state properties of Shotcrete 3d-Printed elements, in: RILEM International Conference on Concrete and Digital Fabrication, XXX, 2022.
[37] L. Lachmayer, R. Dörrie, H. Kloft, A. Raatz, Process control for additive manufacturing of concrete components, in: RILEM International Conference on Concrete and Digital Fabrication, Springer, 2022, pp. 351–356, https://doi.org/10.1007/978-3-031-06116-5-52.